

Macroscopic magnetic hardening due to nanoscale spinodal decomposition in Fe–Cr

V. Vojtech^a, M. Charilaou^b, A. Kovács^c, A. Firlus^a, S.S.A. Gerstl^{a,d}, R.E. Dunin-Borkowski^c, J.F. Löffler^{a,*}, R.E. Schaublin^{a,*}

^a Laboratory of Metal Physics and Technology, Department of Materials, ETH Zurich, 8093 Zurich, Switzerland

^b Department of Physics, University of Louisiana at Lafayette, Lafayette, LA 70504, USA

^c Ernst Ruska-Centre (ER-C) for Microscopy and Spectroscopy with Electrons, Peter Grünberg Institute, Forschungszentrum Jülich, 52425 Jülich, Germany

^d Scientific Center for Optical and Electron Microscopy, ETH Zurich, 8093 Zurich, Switzerland

ARTICLE INFO

Article history:

Received 10 April 2022

Revised 29 July 2022

Accepted 12 August 2022

Available online 13 August 2022

Keywords:

Fe–Cr

Phase decomposition

Atom probe tomography

Lorentz transmission electron microscopy

Magnetism

Hardness

Fusion reactor

ABSTRACT

The Fe–Cr alloy system is the basis of ferritic steels, which are important structural materials for many applications, including their use in future fusion reactors. However, when exposed to elevated temperatures and radiation, the Fe–Cr system can undergo phase separation, resulting in Fe-rich (α) and Cr-rich (α') nanoscale regions. This in turn generates the so-called “475 °C embrittlement” and modifies the magnetic properties. The correlation between the microstructural and magnetic changes is however poorly understood, which currently prevents the possibility of assessing the material in a non-destructive way by magnetometry. Here, we study the microstructural decomposition of an Fe–40Cr alloy induced by annealing at 500 °C for extensive time scales and its impact on the magnetic properties using magnetometry and advanced experimental methods, such as atom probe tomography, transmission electron microscopy (TEM), and micromagnetic simulations. Upon annealing, the alloy rapidly exhibits a spinodal decomposition morphology with a typical length scale of about 10 nm. With increasing annealing time, the hardness assessed by Vickers testing, the magnetic saturation, and the coercivity increase, which correlates with an increase in α -volume fraction and the system's heterogeneity. The magnetic domain patterns imaged by TEM and interpreted with the help of micromagnetic simulations reveal at the nanometer scale the impact of decomposition on the magnetic response of Fe–Cr.

© 2022 The Authors. Published by Elsevier Ltd on behalf of Acta Materialia Inc.

This is an open access article under the CC BY license (<http://creativecommons.org/licenses/by/4.0/>)

1. Introduction

The iron–chromium (Fe–Cr) binary alloy system is essential in engineering materials because it serves as a basis for steels and in particular ferritic steels. These steels are employed in a number of applications due to the combination of cost-effectiveness, extended corrosion resistance, and good thermal and mechanical properties. Among others, these materials are considered for the offshore marine environment [1], gas power plants [2], nuclear fission reactors [3], and future fusion reactors [4]. However, at elevated temperatures, these materials can undergo phase separation, which leads to the so-called “475 °C embrittlement” [5]. This Fe–Cr decomposition, which occurs depending on temperature for Cr contents beyond about 14 wt.% [6], consists of a coherent mixture of Fe-rich (α) phase and Cr-rich (α') phase regions. The effect must in par-

ticular be considered in nuclear power plants, because a constant neutron flux accompanies the high operating temperatures and additionally accelerates phase separation [7–9]. This leads to severe hardening and embrittlement [10], which may ultimately generate structural failure.

The α – α' decomposition in Fe–Cr occurs either via nucleation and growth or via spinodal decomposition, depending on the overall Cr concentration [6], with a boundary between them at about 25–30 wt.% Cr [11]. Note that the study of Fe–Cr phase separation is an active research area for the remaining lack of understanding on e.g. this boundary, and the exact shape of the miscibility gap in the Fe–Cr phase diagram is being constantly re-evaluated.

Many studies have focused on the Fe–Cr decomposition induced by annealing, deploying both experimental and computational methods [8,12–14], with the resulting microstructure described by the composition, morphology and size of the α' -phase regions. Substantial work has also been dedicated to the assessment of phase decomposition induced by irradiation [7,9,15–17]. Such irradiation experiments are important for applications in nu-

* Corresponding authors.

E-mail addresses: joerg.loeffler@mat.ethz.ch (J.F. Löffler), robin.schaublin@mat.ethz.ch (R.E. Schaublin).

clear power and in particular future fusion reactors, but obtaining an understanding of the effects of phase separation in such conditions, and in turn its impact on the material's properties, is more complex due to the synergistic effect of phase separation and irradiation-induced lattice damage.

The material's hardening and embrittlement upon decomposition, which stem from the lowering of dislocation mobility by the presence of the α' regions, have been a major driving force for studying the decomposition process in detail. Early studies in the 1950s [1] were limited by spatial resolution, which was not sufficient to shed light on the microstructural details of the decomposition. With the advent of atom probe tomography (APT) in the 1990s, such information became accessible, and many studies have since then focused on the change in mechanical behavior of Fe–Cr upon α – α' phase separation, induced either purely thermally [18–22] or via irradiation [15,23–25]. In the same timeframe, molecular dynamics simulations were conducted to understand the detailed impact of idealized nanoscale α' precipitates on the mobility of dislocations, revealing that they are rather weak obstacles [26–29]. Nevertheless, there is still a lack of quantitative understanding of how the actual decomposed microstructure impacts the properties of Fe–Cr.

A key aspect of Fe–Cr that can be associated with its structural state and mechanical properties is the magnetic state. In fact, a study by Tissot et al. [8] showed that in the microstructure analysis of decomposed Fe–19 at.% Cr, the Cr-rich particles had to be considered non-magnetic above 70 at.% Cr, in order to match APT and small-angle neutron scattering results.

Fe–Cr in solid solution possesses many different magnetic states, ranging with increasing Cr content [30,31] from ferromagnetic [32,33] to more complex states, such as a spin-glass state [34]. Most of the work done so far in this area has mainly focused on understanding the magnetism at the atom level [32,35–38]. Some works reported magnetic hysteresis loops, which showed an increase in coercivity and a decrease in remanence upon increasing Fe–Cr phase separation, but no satisfactory explanation of those effects in relation to the details of the decomposing microstructure was provided [39–42]. Recently, Chapman et al. [43] investigated via spin-lattice magnetic molecular dynamics the behavior of idealized nanoscale α' precipitates in an α matrix. They provided important first insights into the magnetization, susceptibility and Curie temperature of phase-separated Fe–Cr in relation to its local microstructure, and showed that the susceptibility of Fe atoms is enhanced at the α – α' interface. However, important questions regarding the effect of phase separation on the magnetic state and its response to external fields in a real decomposed microstructure remain open. Deriving a correlation between such microstructures and their magnetic state may lead to a fundamental understanding of their magnetic properties, and potentially to the development of non-destructive sensing techniques for industrial steels. This may eventually serve in preventing damage to structures made of such steels and thus to human life.

In this study, we focused on Fe–Cr with the goal of associating the changes in microstructure induced by thermal annealing to the changes in magnetic properties, with a correlation to hardness changes assessed by Vickers testing. An Fe–Cr alloy with 40 wt.% Cr was chosen for the anticipated strong effect of its microstructural decomposition on magnetic properties, compared to alloys with lower Cr content. This is, on the one hand, due to the large Cr content, and, on the other hand, due to the initial rapid microstructural change that relates to the spontaneous character of spinodal phase separation and does not involve a stable nucleus. The annealing is performed at 500 °C for up to 2016 h. The structure and composition changes are assessed by 3D atom probe tomography (APT) reconstruction correlated with magnetic measurements, focusing on the magnetic saturation and coerciv-

ity obtained by bulk magnetometry. In addition, magnetic imaging using transmission electron microscopy (TEM) methods has been performed to study the local impact of decomposition on the magnetic domain state and in particular on the magnetic domain-wall (DW) width. The interpretation of the results was supported by micromagnetic simulations, deploying 3D APT reconstruction to generate the simulation sample. The magnetic induction maps obtained in this way were then used to simulate the corresponding TEM magnetic images. They were matched to the experimental observations, which allowed us to close the gap between simulations and experiments at the microscopic level. Finally, we combine the experimental results from the macroscopic magnetic saturation and coercivity measurements with high-resolution tomography and electron-based magnetic imaging in concert with micromagnetic simulations, to obtain insight into the fundamental microstructural phenomena that are at the origin of the macroscopic magnetic changes.

2. Materials and methods

2.1. Experimental methods

Fe–Cr with 40 wt.% Cr (41.7 at.% Cr) was prepared with Fe from Alfa Aesar GmbH & Co KG (99.97 wt.% purity) and Cr from Materials Research S.A. (99.996 wt.% purity) by arc melting the constituents in a Ti-gettered 99.999% Ar atmosphere in the form of 20 g button-shaped ingots. Samples were then cut with a diamond saw, wrapped in Ta foil to capture remaining oxygen, enclosed in Ar-filled quartz tubes, and annealed at 850 °C for 5 h to obtain a homogeneous solid solution. They were then air-cooled, sealed in separate quartz tubes under the same conditions as above, and annealed at 500 °C for 240, 480, 1008, and 2016 h with subsequent air cooling. This resulted for all annealing conditions in microstructures with elongated grains of several hundreds of μm in size and with a low density of defects.

The samples for APT analysis were prepared in the form of needles using a standard lift-out procedure with a focused-ion beam scanning electron microscope (FIB-SEM) FEI Helios 600i of the scientific center for optical and electron microscopy (ScopeM) of ETH Zurich, applying 30 kV Ga^+ ions for cutting, and finishing with 5 kV Ga^+ ions showering to minimize Ga implantation and radiation-induced crystal lattice damage in the free surfaces produced during cutting. Final apex was around 50 nm in diameter. For the APT analysis, the Cameca LEAP 4000X-HR instrument of ScopeM was used in standard voltage mode, with a specimen temperature of 23 K, a detection rate of 0.2%, a pulse frequency of 200 kHz, and a pulse fraction of 15%.

A 3D grid was defined by a cubic voxel of 0.8 nm per side and a delocalization of 2.5 nm was used. The amplitude of the Cr-rich fluctuations was assessed by the proxigram method [44] based on isoconcentration surfaces, applying a bin size of 0.2 nm. The same method was used to describe the width and slope of the interface between α and α' regions. The wavelength of the Cr-concentration fluctuations was obtained according to the method reported by Zhou et al. [13], where the maximum of the corresponding radial distribution function (RDF) beyond that at the origin indicates the wavelength of the spinodal structure.

The coercivity at room temperature was measured on bulk samples in the form of lumps of 5 g, using the coercimeter CR/03 (Laboratorio Elettrofisico). For magnetometry, specimens of about 15 mg were extracted. Magnetization measurements were performed at 2 K in a vibrating sample magnetometry mode of 14 Hz, using a superconducting quantum interference device (SQUID) in a magnetic property measurement system (MPMS3) of Quantum Design in a field range of $-0.5 \text{ T} \leq \mu_0 H \leq 0.5 \text{ T}$, where μ_0 is the vacuum permeability and H is the magnetic field.

Mechanical properties were assessed by Vickers hardness testing, which was performed according to the method presented in [45]. The testing was done on single grains with an applied load of 0.1 kg and a dwell time of 15 s. The resulting indent sizes were about 20 to 40 μm .

TEM specimens were prepared in the form of electron-transparent lamellae by FIB-SEM with the FEI Helios 600i at ScopeM, applying the same conditions as above. Specimens were extracted from grains whose orientation was close to the (001) axis, as checked by electron backscatter diffraction (EBSD) using an SEM Quanta 200F TFS of ScopeM. This allows for lamellae with (001) direction, which is the magnetic easy axis, to be oriented in-plane. The lamellae thickness (of around 70 nm) was measured by the conventional log-ratio method using electron energy-loss spectroscopy (EELS), which was performed in a spherical aberration-corrected TEM JEOL grand ARM of ScopeM and operated at 300 kV.

The magnetic imaging in TEM, deploying Fresnel imaging and holography, was carried out using an aberration-corrected microscope (FEI Titan 60–300) operated at 300 kV at ER-C. For Fresnel imaging, or Lorentz TEM (LTEM), the required magnetic-field free environment (<0.1 mT) around the specimen was obtained by turning the microscope's objective lens off (Lorentz mode) and using the first transfer lens of the aberration-corrector unit as Lorentz lens. The defocused Fresnel images of the DWs in Fe–Cr specimens were recorded using a direct electron detecting camera (GATAN K2 IS) [46]. The typical defocus value was 1 mm. Off-axis electron holography (EH) was used to quantify the magnetic flux inside the specimens [47] and to determine the DW width. The electron holograms were acquired using a single electron biprism inserted into one of the conjugated image planes of the microscope and operated at 95 V, which forms holograms with 3.11 nm fringe spacing and approximately 30% fringe contrast. Phase images and magnetic induction maps were reconstructed from the holograms using a custom-made software [48] based on the software Semper [49].

The DW width δ_w was determined using the phase-gradient $\partial\phi/\partial x$ map, where ϕ is the phase shift and x is the spatial dimension perpendicular to the DW. The step function $y(x)$, describing the phase gradient across the DW, was fitted with

$$y = y_0 \pm a \tanh\left(\frac{x - x_0}{w}\right),$$

where y_0 , a , x_0 and w are constants obtained from the fit. The DW width is then estimated by $\delta_w = \pi w$.

2.2. Micromagnetic simulations

Modeling of the magnetic state at the nanoscale in the Fe–Cr microstructure in the solid-solution or decomposed state was performed via micromagnetic simulations, using the software Mumax3 [50]. The sample was decomposed in nanoscale cubic cells and the magnetic moment, \mathbf{m} , of each cell was calculated through minimization of the material's total energy density. The total energy density, E , of a magnetic material with cubic symmetry is:

$$E = A \sum_i (\nabla \mathbf{m}_i)^2 - \mu_0 M_s \mathbf{H} \cdot \mathbf{m} + K_1 (\alpha_x^2 \alpha_y^2 + \alpha_x^2 \alpha_z^2 + \alpha_y^2 \alpha_z^2) - \frac{1}{2} \mu_0 M_s \mathbf{H}_d \cdot \mathbf{m},$$

where A is the exchange stiffness, $\mathbf{m} = \mathbf{M}/M_s$ is the unit vector of the local magnetic moment with saturation magnetization M_s , K_1 is the first-order cubic anisotropy constant, α_i is the directional cosinus with respect to the crystal axis, \mathbf{H} is the applied external field vector, and \mathbf{H}_d is the local field vector due to magnetostatic dipole-dipole interactions.

Simulations of the magnetization $M(H)$ curves were performed by sweeping the external magnetic field in the range of $-1 \text{ T} \leq$

$\mu_0 H \leq +1 \text{ T}$ and minimizing the total energy density at each field strength. For the minimization, we used the steepest conjugate gradient method implemented in Mumax3 [49]. The material parameters for each phase were taken as much as possible from the literature for the Cr contents measured in the present study. The exchange stiffness A derived from the Curie temperature T_C and the lattice constant a were obtained via the relation $A \propto \frac{T_C k_B}{a}$, and the exchange length was calculated via $\delta_{\text{ex}} = 2\sqrt{A/\mu_0 M_s^2}$. In order to have a direct comparison between the simulations and the magnetometry measurements, the simulation sample was made as a cube of 400 nm per side and discretized in cubic cells of 2 nm a side. As to the LTEM imaging experiments, the corresponding simulation object was set to have dimensions comparable to the TEM FIB lamella, i.e., 2048 nm \times 1024 nm \times 64 nm, and the mesh was discretized in cubic cells with a side length of 2 nm.

The α' precipitation structure, having the typical percolating morphology of spinodal decomposition, was approximated by a spatial random distribution of nanoscale Fe- or Cr-rich ellipsoidal precipitates, with a respective composition corresponding to the experimentally measured one. The randomness allowed the generation of precipitates that would in places overlap, thus making an overall precipitation structure that percolates to a certain degree. The average diameter of the precipitates was either 10, 15 or 20 nm, so as to test varying Cr-content fluctuation wavelengths. The ellipsoids size in 3 dimensions was set randomly around these values and according to a Gaussian distribution with a standard deviation of $\pm 2 \text{ nm}$. The number of precipitates was adjusted to obtain in total, accounting for their overlap, the alloy's nominal composition of 40 wt.% Cr.

2.3. Fresnel image simulation

The magnetization model produced by the micromagnetic simulations was applied to simulate the Fresnel images of DWs in order to verify the experimental results. This procedure uses the outcome of the micromagnetic simulations as input for subsequent simulations that are based on the calculation of the electron beam's interaction with the local magnetic moments [51] as it travels through the sample. It is implemented in the software Excalibur [52], which was used in the present work.

3. Results

3.1. Microstructural analysis of phase separation

Fig. 1 summarizes the APT results and their quantitative analysis for the Fe–40 wt.% Cr alloy annealed at 500 $^\circ\text{C}$ for 1008 h and 2016 h. After annealing, APT reveals a clear separation into Fe-rich and Cr-rich regions, as shown in the 3D reconstruction. The Cr isosurfaces for a threshold of 60 wt.% Cr are represented by the green surfaces in Fig. 1a for 1008 h of annealing. Fig. 1b shows a magnified view of it. It exhibits a structure typical of spinodal decomposition, with percolating Cr-rich α' vein-like features, interspersed by the Fe-rich α structure, all having visually the same length scale. Similar features are observed in the sample annealed at 500 $^\circ\text{C}$ for 2016 h, shown in Fig. 1c and d. There is however a clear difference between them, with the Cr-rich features becoming larger and better defined after 2016 h of annealing.

There is also a clear visual difference in the shape of the corresponding RDF curves (Fig. 1e) and proxigrams (Fig. 1f). The difference in structure is further confirmed by the quantitative analysis of the wavelength and amplitude of the fluctuations in Cr content, and the width and slope of the interface between the α and α' regions, defined as having a low and a high Cr content, respectively, as explained in the following.

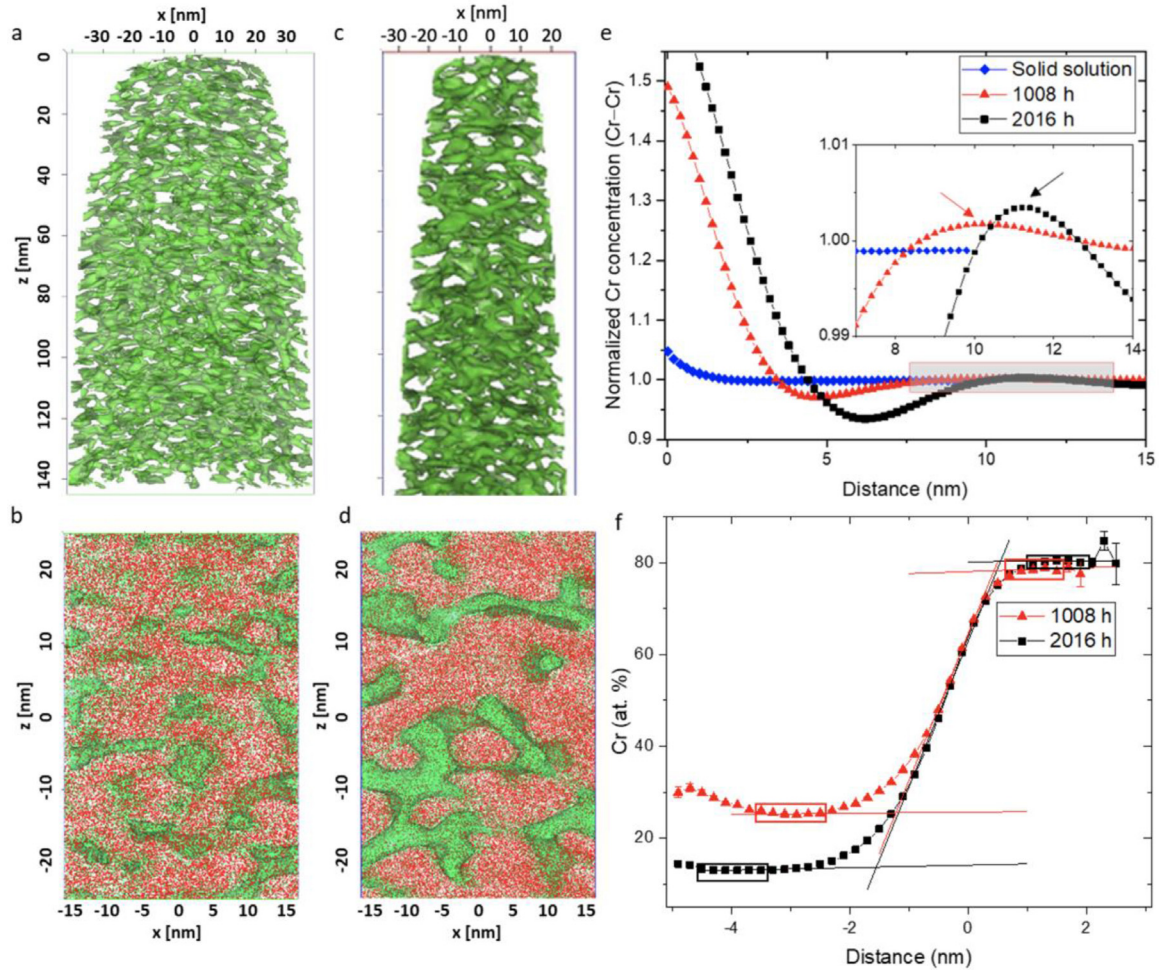


Fig. 1. APT results of the Fe-40 wt.% Cr alloy in three conditions: solution heat-treated, and annealed at 500 °C for 1008 h and 2016 h. (a, c) 3D reconstruction displaying the 60 wt.% Cr isosurface after annealing for 1008 h and 2016 h, respectively. (b, d) Magnified 5-nm thick slice through it, where red depicts Fe atoms and green depicts Cr atoms. (e) RDFs of the three conditions, where the arrows in the inset indicate the maxima of the RDF curves, and (f) proxigrams of the samples annealed for 1008 h and 2016 h. The Cr concentration in the RDF is normalized to the Cr concentration of the bulk alloy. In (f), $x = 0$ is set at the 60 wt.% Cr α - α' interface.

Table 1

Characteristics of the spinodally decomposed Fe-Cr alloy containing 40 wt.% Cr after annealing at 500 °C for 1008 h and 2016 h, as deduced from the APT measurements presented in Fig. 1.

	α Cr content (at.%)	α' Cr content (at.%)	Wavelength (nm)	α - α' interface width (nm)	α - α' interface slope (at.% nm ⁻¹)
1008 h	28.6	76.0	10.2	1.6	30.0
2016 h	13.0	80.0	11.2	2.0	33.8

After 1008 hours of annealing, the average around the α and α' Cr concentration extremum deduced from the corresponding proxigram (Fig. 1f) is respectively 28.6 and 76.0 at.%. After 2016 hours, in α it decreases to 13.0 at.% whereas in α' it increases to 80.0 at.%. The measured wavelength of the Cr-rich fluctuations is 10.2 and 11.2 nm for respectively the 1008 h and 2016 h annealed samples, whereas for the solid-solution sample no maximum was detected in the RDF curve beyond the one at the origin, which is typical of a well-homogenized or random solid solution.

The α - α' interfacial thickness was measured as the distance between intersections of a linear fit in the center of the interfacial region and the linear fits of the Cr concentration plateaus in the α and α' phases, as illustrated in Fig. 1f by the corresponding straight lines. After 1008 h of annealing the measured thickness of the interface was 1.6 nm, while it was 2.0 nm after 2016 h. The slope of

the interface was respectively 30.0 at.% nm⁻¹ and 33.8 at.% nm⁻¹. The results are summarized in Table 1.

3.2. Hardness and magnetometry

Fig. 2 shows the measured magnetization (Fig. 2a) and coercivity (Fig. 2b) of the Fe-Cr alloy with 40 wt.% Cr as a function of annealing time at 500 °C, starting with the solid-solution state. After phase separation the apparent saturation magnetization at an external field of 400 kA m⁻¹ increases from 990 kA m⁻¹ in solid solution to 1037 kA m⁻¹ after 1008 h of annealing and subsequently it decreases to 1010 kA m⁻¹ after 2016 h.

Conversely, the coercivity exhibits an initial strong increase from the solid-solution state to the state of 240 h of annealing at 500 °C, followed by a more moderate but relatively constant in-

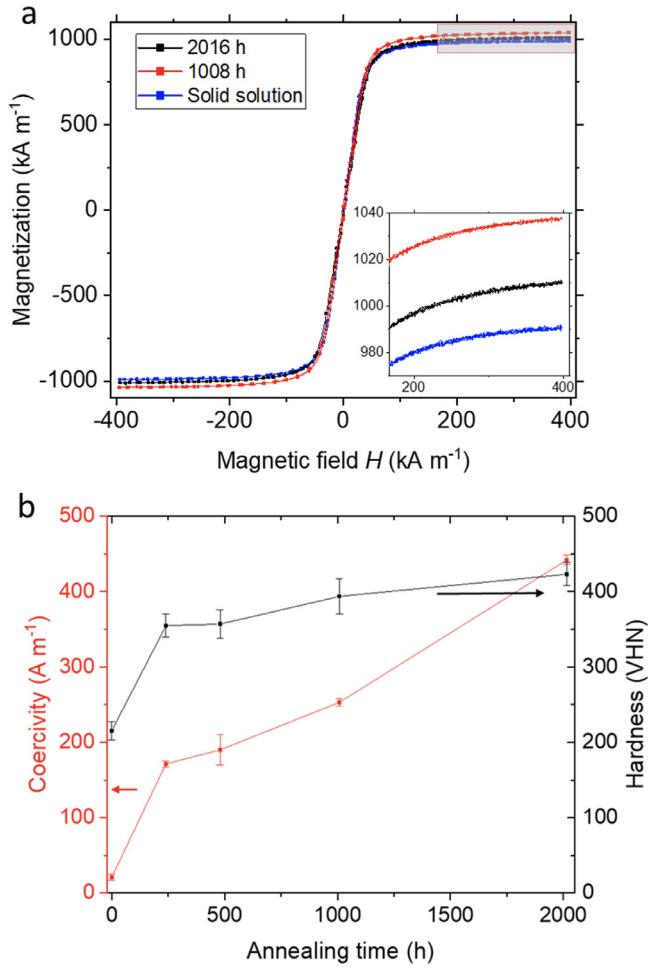


Fig. 2. (a) Magnetization curves of the Fe-40 wt.% Cr alloy for the solution heat-treated state and after annealing at 500 °C for 1008 h and 2016 h; inset: magnified view of the top-right shaded area. (b) Magnetic coercivity and Vickers hardness of the Fe-40 wt.% Cr alloy as a function of annealing time at 500 °C.

crease with increasing annealing time. Upon annealing the coercivity increases by a factor of 20, from 21 A m⁻¹ (≈ 0.03 mT) for the solid-solution state to 442 A m⁻¹ (≈ 0.56 mT) after 2016 h of annealing.

The Vickers hardness as a function of annealing time at 500 °C, as shown in Fig. 2b, presents a similar behavior as the coercivity: it rapidly increases after 240 h of annealing, followed by a slower increase that tends towards saturation, but does not seem to reach it after 2016 h of annealing. The increase in hardness beyond 240 h of annealing is smaller than the coercivity increase. This is reflected in a two-fold increase in hardness, from 215 ± 12 VHN for the solid-solution state to 425 ± 14 VHN after annealing for 2016 h, compared to a 20-fold increase in coercivity over the same time of annealing.

3.3. Micromagnetic simulations

To gain insight in what caused the changes in magnetic properties down to the nanoscale, micromagnetic simulations were performed on the Fe-40 wt.% Cr alloy in the solid-solution state and in the decomposed state following annealing at 500 °C for 2016 h. The corresponding magnetic properties deployed in the simulations are given in Table 2 and the results are presented in Fig. 3.

In the simulations, two mirror microstructures were tested: (i) Cr-rich precipitates in an Fe-rich matrix and (ii) Fe-rich precipitates in a Cr-rich matrix. As shown in Fig. 3, the experimental results for

Table 2

Magnetic properties of the Fe-40 wt.% Cr alloy in solid solution, and of the Cr-rich α' phase and Fe-rich α phase after decomposition, following annealing at 500 °C for 2016 h and considering the as-measured compositions, i.e. 80 and 13 wt.% Cr, respectively. Saturation magnetization, M_s [53]; Curie temperature, T_C [6]; exchange stiffness, A [54]; and exchange length, δ_{ex} .

	M_s (kA m ⁻¹)	T_C (K)	A (pJ m ⁻¹)	δ_{ex} (nm)
Fe-40 wt.% Cr	990	750	15	5.6
Fe-80 wt.% Cr	240	80	1.6	6.6
Fe-13 wt.% Cr	1420	1000	20	4.0

$M(H)$ agree well with the simulation case (i), while case (ii) revealed a large change in susceptibility (not shown) between the solid-solution and phase-separated states. The magnitude of the susceptibility change in the latter case does not correspond to the experimental measurements.

The representative model structure of decomposed Fe-Cr with an α matrix containing α' precipitates of 10 nm in diameter is shown in Fig. 3a. The simulated magnetization of this structure (Fig. 3b) is in good agreement with the experimental data (Fig. 2a), both exhibiting no significant change in susceptibility with annealing.

Simulations of the magnetization with the same microstructure but with a magnetocrystalline anisotropy of $K_1 = 30$ kJ m⁻³, instead of $K_1 = 0$ used in the previous simulation, yielded no difference in the curve shape, indicating that the effect of magnetocrystalline anisotropy on the macroscopic magnetic properties of phase-separated Fe-Cr is negligible. This may be explained by the fact that the system's magnetocrystalline anisotropy is much smaller than its magnetostatic energy density, $\mu_0 M_s^2/2$. We also explored the possible effect of exchange interaction between the two phases, but such interphase exchange can be neglected because of the weak magnetism of the Cr-rich phase, which contributes little to the overall magnetic state and its response.

3.4. TEM magnetic imaging

To explore the effect of the experimentally observed wavelength changes in Cr-content fluctuation as a function of annealing time, we conducted simulations with different precipitate sizes, namely 10, 15 and 20 nm, but did not observe changes in the magnetization curve (not shown).

To get a deeper understanding of the relationship between the microstructure and magnetic properties, we performed magnetic imaging in TEM on the Fe-40 wt.% Cr alloy in the solid-solution state and after annealing at 500 °C for 1008 h (not shown) and for 2016 h (Fig. 4). First, Fresnel defocus images were recorded at the magnetic remanence state in order to visualize the magnetic domains. The dark and white lines in Fig. 4a,b and Fig. 4d,e indicate DWs, revealing a clear difference in the domain pattern between the solid-solution and phase-separated states. In the phase-separated state the domain size strongly decreased (Fig. 4d), with a considerably higher number of DWs compared to the solid-solution state (Fig. 4a). The domain size for the solid solution is approximately 5 μ m and decreases to sub-micrometer, at 0.9 μ m after 2016 h of annealing. It should be noted that the absolute values of the magnetic-domain characteristics depend on the crystal orientation and dimensions of the lamellae. Both lamellae had a normal close to $\langle 001 \rangle$, and respectively a size of about 4.8×6.1 and $5.0 \times 6.1 \mu\text{m}^2$ and a thickness of about 74 and 70 nm. Given the small differences between them, we assume that the observed decrease in domain size by almost one order of magnitude stems mainly from the change of the material's microstructure.

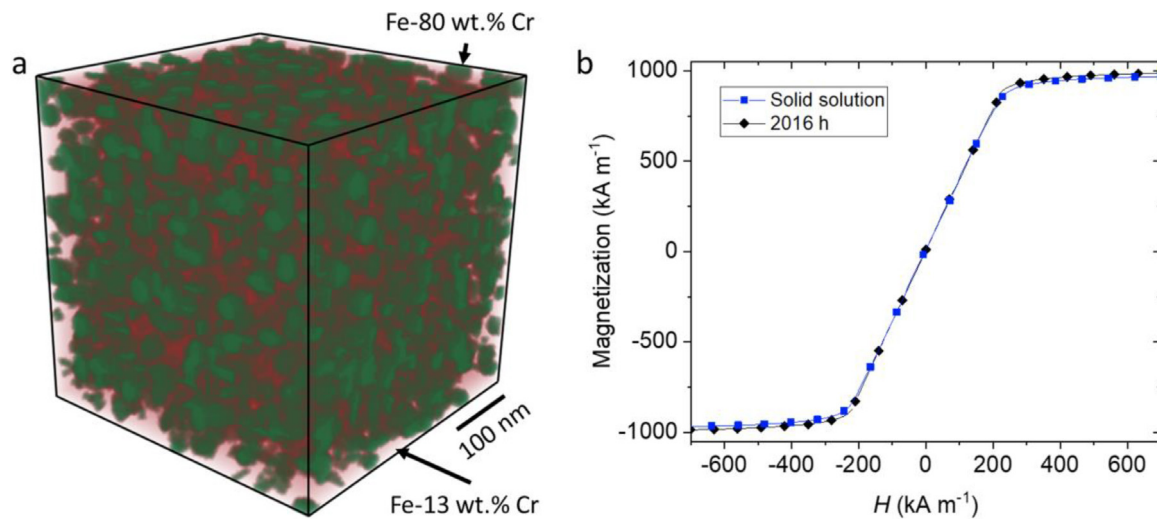


Fig. 3. Micromagnetic simulations of the magnetic response for Fe-40 wt.% Cr in solid solution and after annealing at 500 °C for 2016 h. (a) 3D view of the simulation input cubic sample of 400 nm a side, which represents the percolating Fe-rich α and Cr-rich α' regions observed experimentally after annealing (Fe: red, Cr: green). (b) Simulated magnetization curves as a function of applied magnetic field for the two conditions.

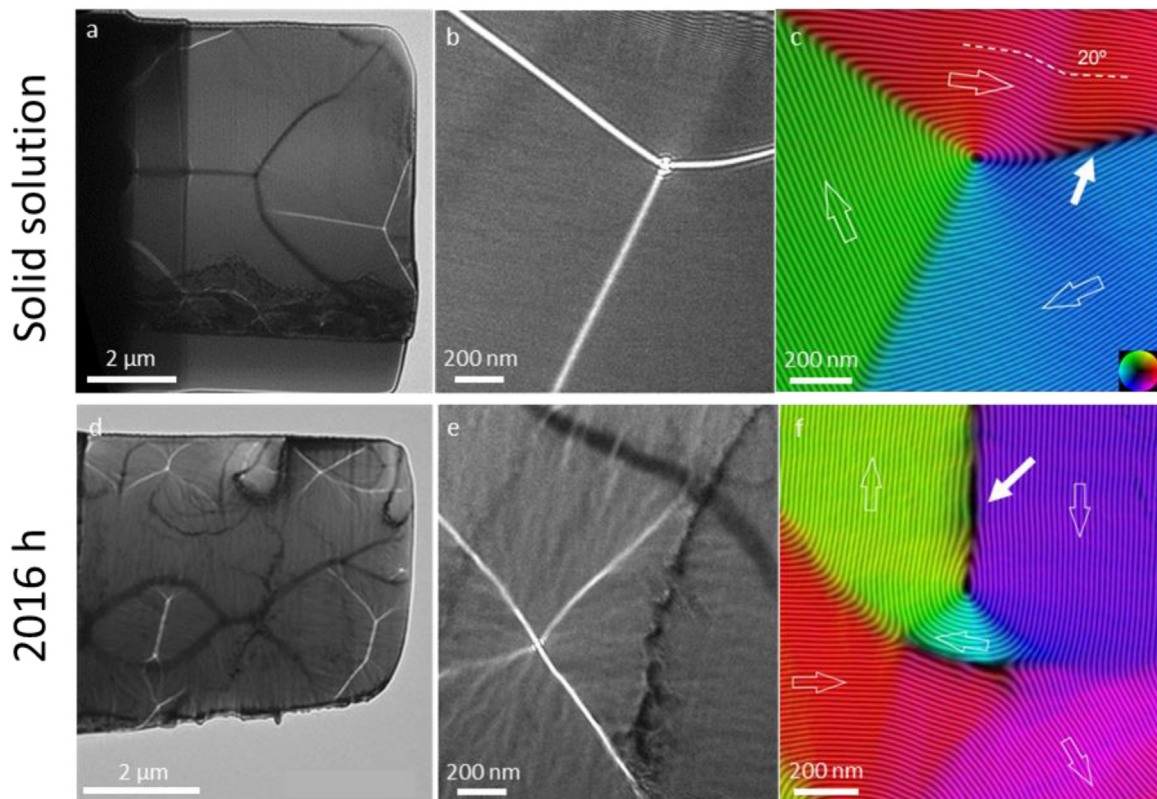


Fig. 4. TEM magnetic imaging of the domain pattern in Fe-40 wt.% Cr after (a–c) solution heat-treatment and (d–f) annealing at 500 °C for 2016 h. Magnetic DWs in Fresnel defocus (1 mm) images (a,b,d,e) appear with black and white contrast. The images shown in (b,e) are magnified parts of regions from (a) and (d). (c,f) Magnetic induction maps of characteristic regions from specimens of (c) the solid-solution state and (f) after annealing at 500 °C for 2016 h, extracted from off-axis electron holography. The contour lines and colors indicate the in-plane magnetic field strength and direction around the intersection of three DWs. The contour spacing is π rad. Solid arrows in (c,f) mark the regions used to determine the DW width.

Importantly, Fig. 4e reveals a magnetic ripple contrast between well-defined DWs, which has so far not been observed in magnetic single-crystals. In contrast to high-angle DWs, magnetic ripples are small-angle variations of the magnetization and the characteristic texture is orthogonal to the average magnetization direction. Its presence in the decomposed Fe-40 wt.% Cr sample annealed

for 2016 h suggests a perturbation in local magnetic anisotropies. No ripple contrast was observed between the DWs for the solid-solution sample, where the magnetic domains are mostly smooth and featureless, as shown in the Fresnel images in Fig. 4a,b.

The magnetic induction and quantitative measurement of the DW width of the Fe-40 wt.% Cr alloy in the solid-solution state and

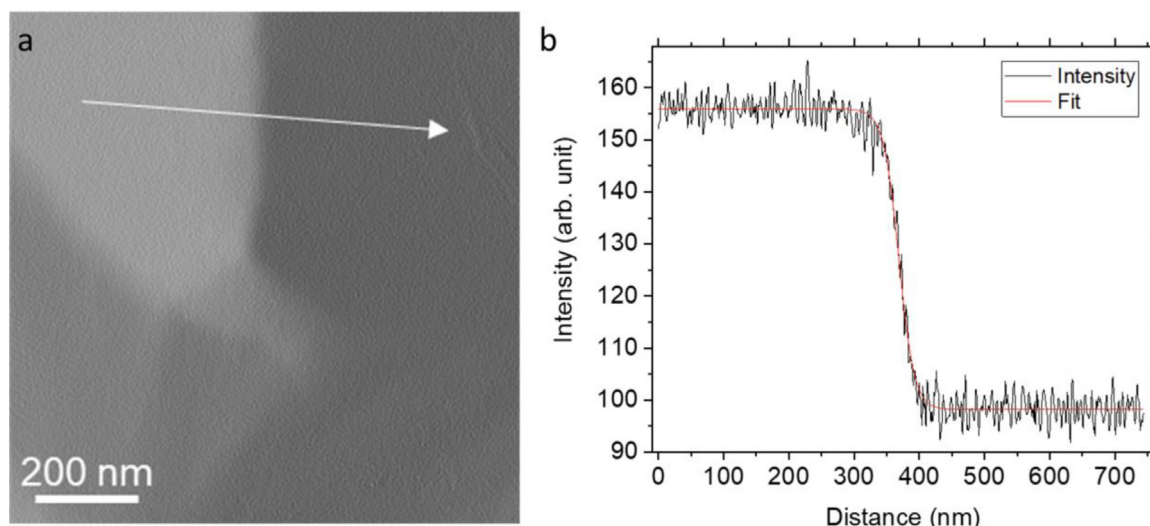


Fig. 5. DW-width measurement using off-axis electron holography in the TEM. (a) Map of phase-shift differential calculated orthogonal to the DW of an Fe-40 wt.% Cr sample annealed at 500 °C for 2016 h. The white arrow indicates the direction of the intensity profile presented in (b). A fit to the intensity profile allows for an estimate of the DW width as 74 ± 5 nm.

after annealing for 1008 and 2016 h was further evaluated using off-axis electron holography (EH), which allows to map the electron phase shift of the in-plane magnetic vector potential in the sample [48]. Fig. 4c,f shows the magnetic induction maps of flux closures in the samples. Note the small- and long-range magnetic flux variations (marked with a dashed line and “20°” in Fig. 4c) within the domains of the solid-solution sample. These features form to reduce the wall energy, which would be highest for 180° DWs. However, only angles of up to 160° between two domains were measured for the solid-solution state. In contrast, 180° DWs were frequently observed in the samples annealed for 1008 h (not shown) and 2016 h (Fig. 4f). The presence of these high-angle DWs in the annealed samples suggests an increased magnetic anisotropy compared to the solid solution. Because of the low DW density in the solid-solution sample and the experimental constraints of off-axis EH, the DW triple junction was further analyzed (Fig. 4b, c). Here, a section with a 160° DW was used to determine the DW width using off-axis EH. In the phase-separated conditions, the higher DW density allowed us to make measurements of the DW width in portions close to 180° (Fig. 4f). The DW widths were determined by fitting the intensity change of the phase-shift differential calculated orthogonal to the DW, as shown in Fig. 5. It was found that the DW width remains the same upon initial phase separation, with 87 ± 5 nm in the solid-solution state and 85 ± 5 nm in the samples annealed at 500 °C for 1008 h. However, the DW width decreased to 74 ± 5 nm for the sample annealed for 2016 h. In simple terms, the DW width $\delta \sim \pi \sqrt{A/K}$ scales with the ratio of the exchange stiffness A and anisotropy K . However, in the phase-separated Fe-40 wt.% Cr alloys both are likely to be affected by annealing, which requires a comprehensive analysis beyond the scope of the present study.

4. Discussion

We aim to connect the change in microstructure with the observed changes in hardness, magnetic properties, and magnetic structure. Establishing this connection is a necessary step to open a path towards a non-destructive evaluation of these materials. First, the results and observations of the different compositional, structural, mechanical, and magnetic properties are reviewed, together

with the magnetic imaging and modeling results deduced from both the macro- and microscopic investigations.

4.1. Microstructural evolution during long-term annealing

The spinodal decomposition of an Fe-40 wt.% Cr alloy annealed at 500 °C was characterized using APT by the amplitude and wavelength of the Cr-content fluctuations and the profile of the α - α' interfaces (Table 1). After 1008 h of annealing, the average peak concentration of Cr in both α and α' did not reach equilibrium, as it changed from respectively 28.6 and 76.0 at.% Cr after 1008 h of annealing to 13.0 and 80.0 at.% Cr after 2016 h of annealing. This makes a relative decrease in Cr content in α of about 55% and a relative increase of Cr content in α' of about 5%. Note that in Ref. [45] the Cr peak concentration in α' of the same material annealed at 500 °C for 1008 h was reported to be about 82 at.%, instead of the 76 at.% measured in the present study. The difference stems from the fact that in this earlier work [45] the measurement was made by energy-dispersive X-ray spectrometry (EDS) in the TEM. In this case only the α' regions that exhibit a maximum of Cr are considered, in order to exclude regions of the TEM thin sample that may include overlapping α and α' regions, which inherently biases the resulting composition towards higher Cr contents. With this consideration, the lower Cr peak concentration in α' measured here by APT seems reasonable.

The slope in Cr concentration of the α and α' interface increased from 30.0 to 33.8 at.% nm⁻¹ upon annealing to 2016 h, which corresponds to an increase of about 13%. According to Cahn and Hillard [55], equilibrium in spinodal decomposition is obtained when the interfacial thickness reaches an equilibrium value specific to a given temperature. That state was not attained after 1008 h of annealing at 500 °C, since the measured interface thickness still increased from 1.56 nm to 1.98 nm upon further annealing to 2016 h, which represents a relative increase of 27%.

4.2. Changes in saturation magnetization in relation to phase composition and volume fraction

Regarding the modification of magnetic properties, several factors need to be considered and different aspects generally influence the saturation magnetization and coercivity.

The explanation of the peculiar changes in saturation magnetization may relate to the atomic scale, as the value of magnetic moment on each atom is strongly affected by the surroundings of each atom. In the phase-separated structure we investigate the environment changes locally from a rather diluted Fe–Cr alloy with a concentration as low as 14 at.% Cr to a concentrated alloy containing as much as 80 at.% Cr. According to theoretical works, these regions behave fundamentally different [36,56,57], with a decrease of the saturation magnetization when increasing the Cr content up to 80 wt.%. We thus attribute the initial increase in saturation magnetization to the increase in volume fraction of the Fe-rich phase, as it has a higher saturation value compared to the one of the solid-solution state. The subsequent decrease in saturation magnetization is most probably caused by an increase in volume fraction of the material with a Cr concentration of more than about 75 at.%, where also Fe loses its magnetic moment and is no longer compensated for by the increase in volume fraction of the Fe-rich phase.

Assuming that the saturation magnetization relates only to the fractions of phases with varying Cr content, we calculated the atomic average magnetic moment using the phase fractions deduced from APT and the atomic magnetic moment as a function of the Cr content, as reported by Xiong et al. [6]. To that end, the APT data sample was divided in cubic voxels with a side length ranging from 0.45 to 3.0 nm and the Cr ratio was estimated in each voxel. This yielded a voxel frequency distribution as a function of Cr content set with a bin width of 5 at.%. The frequency distribution of the annealed states presented a bimodal distribution, reflecting the spinodal decomposition into Fe-rich and Cr-rich regions, while the solid-solution state presented a single broad peak centered at around 40 at.%, as expected. The calculation yielded a higher average magnetic moment per atom for the annealed states compared to the solid-solution state, which corresponds to the trend observed in the experimental results. More precisely, for a voxel size of 0.45 nm, the resulting atomic average magnetic moment is 1.666, 1.693 and 1.688 μ_B for Fe-40Cr respectively in solid solution and annealed at 500 °C for 1008 h and 2016 h. It shows the increase of the atomic magnetic moment from the solid-solution state to the annealed states, as well as the slight decrease from 1008 h to 2016 h, as observed in the SQUID measurements.

It should be noted that the change in saturation magnetization is an indicator of changes in microstructure, and subsequently in mechanical properties, as it is an intrinsic property of the material depending solely on the local chemical ordering and not on its macroscopic shape.

4.3. Origin of the coercivity increase in relation to the Fe-rich phase morphology

The change in microhardness shows a concurrent trend with the change in coercivity. Interestingly, the difference between hardness and magnetic coercivity is most pronounced at the first annealing step of 240 h, which may relate to the barrier-free evolution of spinodal decomposition. Subsequently, the coercivity increased significantly with longer annealing times, whereas the hardness only slightly increased, reaching a value of 425 ± 14 VHN after 2016 h of annealing.

The coercivity enhancement is associated with a reduced microstructural length scale of the Fe-rich precipitate-like features. Specifically, the magnetization of the Fe-rich state is confined to a length scale on the order of 10 nm, which is comparable to its exchange length (6.6 nm). In the scenario of Fe-rich precipitates, isolated particles with a size of 10 nm will behave as Stoner–Wohlfarth-type single-domain particles [56], and the coercivity can be assessed as $H_c = H_{an}/2$, where $H_{an} = N_{eff}M_s/2$ is the anisotropy field due to the shape of the precipitates and N_{eff} is the effective demagnetizing factor that depends on the shape (elongation).

Therefore, isolated Fe-rich precipitates will host no DWs and exhibit an enhanced coercivity due to their shape anisotropy. This is, however, limited to largely isolated Fe-rich particles, and therefore only to a small fraction of the real microstructure. In percolating Fe-rich precipitates, DWs will be present, but due to the elongation of the precipitates, N_{eff} will be larger and increase the anisotropy field. This increases the effective anisotropy, K_{eff} , and generates a higher DW energy $E_{DW} \propto \sqrt{AK_{eff}}$, which in turn will also contribute to an increased coercivity. We assume that the dense network of interfaces between the Fe-rich and Cr-rich phases further hinders DW motion, which is necessary for magnetization reversal, due to the large difference of the DW energy between the two phases. The LTEM study revealed that the annealed states contain a higher number density of DWs than the solid-solution state. Because this higher density of DWs is less mobile, the coercivity will increase in the annealed samples.

Given the above, we attribute the increase in coercivity to the reduced length scale of precipitating Fe-rich phases, while the saturation depends stronger on microstructural features, which in turn depend on the degradation stage.

The increased spinodal decomposition with increasing annealing time in conjunction with the correlated coarsening of the α' -phase (see Table 1) reduces the α - α' interfacial surface and broadens the α - α' interfaces by 27%. This results in a decrease in the number of Fe atoms susceptible to favor DW nucleation and propagation and in an increased potential for the interaction of the DWs with the α - α' interfaces. This decoupling of the Fe-rich precipitates upon annealing enhances the coercivity (see Fig. 2), as has been described quantitatively in [58].

In the case of leaner Fe–Cr alloys, such as Fe–Cr containing 20 wt.% Cr, where a nucleation and growth type of α - α' phase separation occurs, with isolated globular α' precipitates in the α matrix, the effect on magnetic properties would be insignificant, as the Fe-rich matrix would favor the magnetic reversal and thus maintain the coercivity to the level of the solid-solution state [59]. We therefore suggest that the key to the change in magnetic properties upon α - α' phase separation is the isolation of the Fe-rich regions stemming from the spinodal type of decomposition.

As described above, the decrease in domain size and the resulting increase in DW density observed by LTEM confirm our understanding of a coercivity increase with continuing phase separation. This combined with the previously described ripple contrast, showing local changes in the magnetization vector within single domains being induced by the isolation of Fe-rich phase regions, suggests that the α - α' interfaces make DW motion more difficult.

4.4. Origin of the ripple contrast

To study the origin of the ripple contrast observed in the Fresnel defocus images in relation to the specimen's magnetic structure, and to exclude potential artefacts due to sample preparation, we created a model of Fe-40 wt.% Cr samples for micromagnetic simulations in the shape and size of a real FIB-prepared lamella, in both the solid-solution state and the decomposed state after annealing at 500 °C for 2016 h, and used the result to simulate the corresponding Fresnel defocus images. The results are presented in Fig. 6, with the respective Figs. 6a and 6b revealing the simulated magnetic induction maps and illustrating the increase in DW density upon decomposition. The simulated Fresnel defocus images obtained from the magnetic induction maps (Fig. 6c,d) agree well with the experimental images presented in Fig. 4, where in the solid-solution state the DWs are well defined and the domains are uniform (Fig. 6c) and in the decomposed state the DWs are more numerous and less well-defined (Fig. 6d). The background in Fig. 6d even reproduces the ripples observed experimentally. Together with the DWs, the simulated images present a remarkable

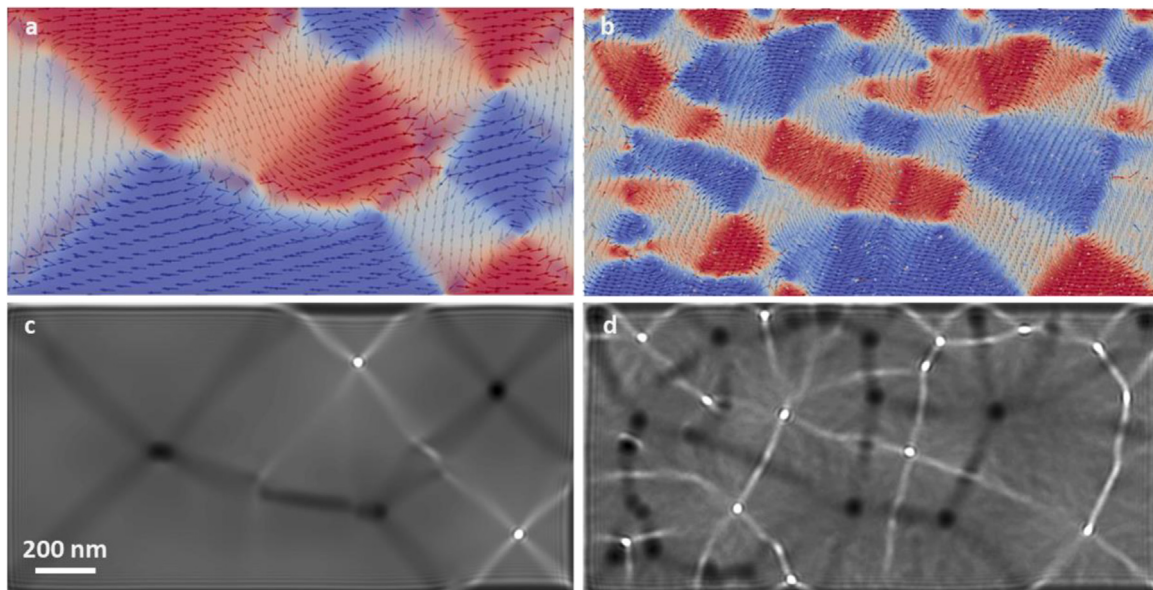


Fig. 6. Results of (a,b) micromagnetic simulation of the magnetic induction map and the corresponding (c,d) TEM Fresnel image simulation of Fe-40 wt.% Cr samples in solid solution and annealed at 500 °C for 2016 h, respectively. Note the presence of a ripple contrast in (d), which matches well the experimental result presented in Fig. 4e.

similarity to the experimental ones, which allows excluding any sort of artefact due to sample preparation. The lower contrast of the ripples compared to the DW contrast indicates that the ripples relate to rather minute changes of the local magnetization direction within the single domains of the specimen. Such a ripple contrast is known to emerge in polycrystalline samples and in the case of high magnetocrystalline anisotropy: it results from different grain orientations that cause a deviation of the local magnetization. Here, the FIB lamella is a single-crystal, i.e., there is only one crystal orientation, which is close to $\langle 001 \rangle$ and is an easy axis of Fe. The ripple contrast results from the local magnetization modulation that alternates between large and low M_s in the Fe-rich and Cr-rich regions and the variation in local magnetization direction associated with the shape anisotropy of the individual precipitates.

The DW analyses by off-axis EH revealed a decrease in DW width towards the value of pure Fe with annealing, which suggests a magnetic anisotropy increase due to the elongated shape of the precipitate-like features. Here one may consider two contributions to the shape anisotropy: (i) the shape of the lamella, which is associated with a global anisotropy $K_g = \mu_0 \bar{M}_s^2 / 4$, where \bar{M}_s is the average magnetization of the lamella, and (ii) a local anisotropy $K_l = \mu_0 N_{\text{eff}} M_s^2$ due to the precipitates. The resulting DW structure is a result of the competition between those contributions and is also affected by the dense interfaces.

5. Conclusions

An Fe–Cr alloy containing 40 wt.% Cr was annealed at 500 °C for times of up to 2016 h to study the alloy's phase decomposition and its impact on the magnetic properties, using APT, magnetometry, magnetic imaging in TEM, and micromagnetic simulations. The related change in mechanical properties was probed by Vickers hardness. Our specific conclusions are the following:

- (1) The Fe–Cr alloy presents upon annealing a spinodal decomposition microstructure made of percolating Fe-rich α and Cr-rich α' regions or veins. Its wavelength ranges up to about 11 nm with an average Cr-peak concentration in α' regions of up to 80.0 at.%. The interface width between the α and α' regions in-

creases from 1.6 to 2.0 nm for an increase in annealing time from 1008 h to 2016 h.

- (2) While the magnetic susceptibility remains constant, the saturation magnetization increases upon annealing to 1008 h, but then decreases with annealing to 2016 h. It relates to the emergence of Fe-rich α -phase regions. The subsequent decrease of the saturation magnetization between 1008 and 2016 h of annealing is related to the increase in Cr-rich phase regions with more than 75 at.% of Cr where Fe loses its ferromagnetic nature.
- (3) The magnetic coercivity increases with increasing annealing time, in relation to the increase in Vickers hardness. The increase is rapid in the first 240 h of annealing and then slows down. It relates to the increasing structural heterogeneity upon annealing and the size and concentration of the α -phase regions.
- (4) LTEM revealed the emergence of a magnetic ripple contrast upon α/α' decomposition. This was reproduced with a micrograph obtained by micromagnetic simulations. The ripple contrast relates to the disruption of magnetic induction lines by the α' regions.
- (5) Because the hardness changes similarly to the magnetic properties upon annealing, the latter can be used to probe in a non-destructive way the changes in mechanical properties of industrial ferromagnetic steels, following a change in microstructure that may be induced by heat or potentially irradiation.

Declaration of Competing Interest

The authors declare that they have no known competing financial interests or personal relationships that could have appeared to influence the work reported in this paper.

Acknowledgments

The authors thank J. Reuteler, ScopeM, ETH Zurich, for help with the FIB work and R. Ulfing, CAMECA Instruments, Madison, WI, USA, for extending the APT RDF range beyond 10 nm. The authors acknowledge funding by the Swiss National Science Foundation (Grants No. 200021–172934 and 200020–207929), and thank the Scientific Center for Optical and Electron Microscopy (ScopeM),

ETH Zurich, for providing access to its facilities. A.K. and R.D.B acknowledge the support by the Deutsche Forschungsgemeinschaft (DFG) through CRC/TRR 270 (Project ID 40553726) and the European Union's Horizon 2020 Research and Innovation Programme (Grant No. 856538, project "3D MAGiC").

References

- [1] R.L. Reuben, Materials in marine technology, Springer, London, 1994, doi:10.1007/978-1-4471-2011-7.
- [2] T. Yukitoshi, K. Yoshikawa, T. Daikoku, F. Masuyama, Experience of high chromium ferritic steel tubes in power plant, J. Mater. Energy Syst. 4 (1982) 99–109, doi:10.1007/BF02898277.
- [3] R.L. Klueh, A.T. Nelson, Ferritic/martensitic steels for next-generation reactors, J. Nucl. Mater. 371 (2007) 37–52, doi:10.1016/j.jnucmat.2007.05.005.
- [4] D.M. Duffy, Fusion power: a challenge for materials science, Philos. Trans. R. Soc. A Math. Phys. Eng. Sci. 368 (2010) 3315–3328, doi:10.1098/rsta.2010.0060.
- [5] R.O. Williams, H.W. Paxton, The nature of aging of binary iron-chromium alloys around 500 °C, J. Iron Steel Inst. 185 (1957) 358–374.
- [6] W. Xiong, M. Selleby, Q. Chen, J. Odqvist, Y. Du, Phase equilibria and thermodynamic properties in the Fe–Cr system, Crit. Rev. Solid State Mater. Sci. 35 (2010) 125–152, doi:10.1080/10408431003788472.
- [7] O. Tissot, C. Pareige, E. Meslin, B. Décamps, J. Henry, Kinetics of α' precipitation in an electron-irradiated Fe15Cr alloy, Scr. Mater. 122 (2016) 31–35, doi:10.1016/j.scriptamat.2016.05.021.
- [8] O. Tissot, C. Pareige, M.H. Mathon, M. Roussel, E. Meslin, B. Décamps, J. Henry, Comparison between SANS and APT measurements in a thermally aged Fe-19 at.%Cr alloy, Mater. Charact. 151 (2019) 332–341, doi:10.1016/j.matchar.2019.03.027.
- [9] O. Tissot, C. Pareige, E. Meslin, B. Décamps, J. Henry, Influence of injected interstitials on α' precipitation in Fe–Cr alloys under self-ion irradiation, Mater. Res. Lett. 5 (2017) 117–123, doi:10.1080/21663831.2016.1230896.
- [10] P.J. Grobner, The 885 °F (475 °C) embrittlement of ferritic stainless steels, Metall. Trans. 4 (1973) 251–260, doi:10.1007/BF02649625.
- [11] P. Hedström, S. Baghsheikhi, P. Liu, J. Odqvist, A phase-field and electron microscopy study of phase separation in Fe–Cr alloys, Mater. Sci. Eng. A 534 (2012) 552–556, doi:10.1016/j.msea.2011.12.007.
- [12] E. Martinez, O. Senninger, C.C. Fu, F. Soisson, Decomposition kinetics of Fe–Cr solid solutions during thermal aging, Phys. Rev. B 86 (2012) 224109, doi:10.1213/ane.0b013e318193c439.
- [13] J. Zhou, J. Odqvist, M. Thuvander, P. Hedström, Quantitative evaluation of spinodal decomposition in Fe–Cr by atom probe tomography and radial distribution function analysis, Microsc. Microanal. 19 (2013) 665–675, doi:10.1017/S1431927613000470.
- [14] S. Novy, P. Pareige, C. Pareige, Atomic scale analysis and phase separation understanding in a thermally aged Fe-20 at.%Cr alloy, J. Nucl. Mater. 384 (2009) 96–102, doi:10.1016/j.jnucmat.2008.10.008.
- [15] V. Kuksenko, C. Pareige, P. Pareige, Cr precipitation in neutron irradiated industrial purity Fe–Cr model alloys, J. Nucl. Mater. 432 (2013) 160–165, doi:10.1016/j.jnucmat.2012.07.021.
- [16] C. Heintze, F. Bergner, A. Ulbricht, H. Eckerlebe, The microstructure of neutron-irradiated Fe–Cr alloys: a small-angle neutron scattering study, J. Nucl. Mater. 409 (2011) 106–111, doi:10.1016/j.jnucmat.2010.09.010.
- [17] W.Y. Chen, Y. Miao, Y. Wu, C.A. Tomchik, K. Mo, J. Gan, M.A. Okuniewski, S.A. Maloy, J.F. Stubbs, Atom probe study of irradiation-enhanced α precipitation in neutron-irradiated Fe–Cr model alloys, J. Nucl. Mater. 462 (2015) 242–249, doi:10.1016/j.jnucmat.2015.04.005.
- [18] S.S. Brenner, M.K. Miller, W.A. Soffa, Spinodal decomposition of Iron-32 at.% chromium at 470 °C, Scr. Metall. 16 (1982) 831–836, doi:10.1016/0036-9748(82)90239-3.
- [19] M.K. Miller, J.M. Hyde, A. Cerezo, G.D.W. Smith, Comparison of low temperature decomposition in FeCr and duplex stainless steels, Appl. Surf. Sci. 87–88 (1995) 323–328, doi:10.1016/0169-4332(95)00497-1.
- [20] V.M. Lopez-Hirata, O. Soriano-Vargas, H.J. Rosales-Dorantes, M.L.S. Muñoz, Phase decomposition in an Fe-40 at.% Cr alloy after isothermal aging and its effect on hardening, Mater. Charact. 62 (2011) 789–792, doi:10.1016/j.matchar.2011.05.012.
- [21] O. Soriano-Vargas, E.O. Avila-Davila, V.M. Lopez-Hirata, N. Cayetano-Castro, J.L. Gonzalez-Velazquez, Effect of spinodal decomposition on the mechanical behavior of Fe–Cr alloys, Mater. Sci. Eng. A 527 (2010) 2910–2914, doi:10.1016/j.msea.2010.01.020.
- [22] P. Hedström, F. Huyen, J. Zhou, S. Wessman, M. Thuvander, J. Odqvist, The 475 °C embrittlement in Fe-20Cr and Fe-20Cr-X (X=Ni, Cu, Mn) alloys studied by mechanical testing and atom probe tomography, Mater. Sci. Eng. A 574 (2013) 123–129, doi:10.1016/j.msea.2013.03.016.
- [23] E.R. Reese, N. Almirall, T. Yamamoto, S. Tumey, G.R. Odette, M. Marquis, Dose rate dependence of Cr precipitation in an ion-irradiated Fe18Cr alloy, Scr. Mater. 146 (2018) 213–217, doi:10.1016/j.scriptamat.2017.11.040.
- [24] F. Soisson, E. Meslin, O. Tissot, Atomistic modeling of α' precipitation in Fe–Cr alloys under charged particles and neutron irradiations: effects of ballistic mixing and sink densities, J. Nucl. Mater. 508 (2018) 583–594, doi:10.1016/j.jnucmat.2018.06.015.
- [25] D. Bhattacharyya, T. Yamamoto, P. Wells, E. Marquis, M. Bachhav, Y. Wu, J. Davis, A. Xu, G.R. Odette, Microstructural changes and their effect on hardening in neutron irradiated Fe–Cr alloys, J. Nucl. Mater. 519 (2019) 274–286, doi:10.1016/j.jnucmat.2019.03.022.
- [26] D.A. Terentyev, G. Bonny, L. Malerba, Strengthening due to coherent Cr precipitates in Fe–Cr alloys: atomistic simulations and theoretical models, Acta Mater. 56 (2008) 3229–3235, doi:10.1016/j.actamat.2008.03.004.
- [27] S.M. Hafez Haghighat, D. Terentyev, R.E. Schaublin, Atomistic simulation of the influence of Cr on the mobility of the edge dislocation in Fe(Cr) alloys, J. Nucl. Mater. 417 (2011) 1094–1097, doi:10.1016/j.jnucmat.2011.01.087.
- [28] R.E. Schaublin, S.M. Hafez Haghighat, Molecular dynamics study of strengthening by nanometric void and Cr alloying in Fe, J. Nucl. Mater. 442 (2013) S643–S648, doi:10.1016/j.jnucmat.2013.04.045.
- [29] S.M. Hafez Haghighat, R.E. Schaublin, D. Raabe, Atomistic simulation of the a0 (1 0 0) binary junction formation and its unzipping in body-centered cubic iron, Acta Mater. 64 (2014) 24–32, doi:10.1016/j.actamat.2013.11.037.
- [30] S.K. Burke, B.D. Rainford, The evolution of magnetic order in CrFe alloys. III. Ferromagnetism close to the critical concentration, J. Phys. F Met. Phys. 13 (1983) 471–482, doi:10.1088/0305-4608/13/2/021.
- [31] E. Fawcett, Spin-density-wave antiferromagnetism in chromium, Rev. Mod. Phys. 60 (1988) 209–283, doi:10.1103/RevModPhys.60.209.
- [32] M.Y. Lavrentiev, K. Mergia, M. Gjoka, D. Nguyen-Manh, G. Apostolopoulos, S.L. Dudarev, Magnetic cluster expansion simulation and experimental study of high temperature magnetic properties of Fe–Cr alloys, J. Phys. Condens. Matter. (2012) 24, doi:10.1088/0953-8984/24/32/326001.
- [33] D. Nguyen-Manh, M.Y. Lavrentiev, S.L. Dudarev, Ab initio and Monte Carlo modeling in Fe–Cr system: magnetic origin of anomalous thermodynamic and kinetic properties, Comput. Mater. Sci. 44 (2008) 1–8, doi:10.1016/j.commatsci.2008.01.035.
- [34] S.K. Burke, R. Cywinski, J.R. Davis, B.D. Rainford, The evolution of magnetic order in CrFe alloys. II. Onset of ferromagnetism, J. Phys. F Met. Phys. 13 (1983) 451–470, doi:10.1088/0305-4608/13/2/020.
- [35] S.M. Dubiel, J. Zukrowski, Mössbauer effect study of charge and spin transfer in Fe–Cr, J. Magn. Mater. 23 (1981) 214–228, doi:10.1016/0304-8853(81)90137-2.
- [36] T.P.C. Klaver, R. Drautz, M.W. Finnis, Magnetism and thermodynamics of defect-free Fe–Cr alloys, (2006) 1–11, doi:10.1103/PhysRevB.74.094435.
- [37] A. Froideval, R. Iglesias, M. Samaras, S. Schuppler, P. Nagel, D. Grolimund, M. Victoria, W. Hoffelner, Magnetic and structural properties of FeCr alloys, Phys. Rev. Lett. 99 (2007) 5–8, doi:10.1103/PhysRevLett.99.237201.
- [38] D. Nguyen-Manh, P.W. Ma, M.Y. Lavrentiev, S.L. Dudarev, Constrained non-collinear magnetism in disordered Fe and Fe–Cr alloys, Ann. Nucl. Energy 77 (2015) 246–251, doi:10.1016/j.anucene.2014.10.042.
- [39] J.N. Mohapatra, Y. Kamada, H. Kikuchi, S. Kobayashi, J. Echigoya, D.G. Park, Y.M. Cheong, Evaluation of sigma phase embrittlement in Fe–Cr alloys by magnetic hysteresis loop technique, Stud. Appl. Electromagn. Mech. 36 (2012) 117–123, doi:10.3233/978-1-60750-968-4-117.
- [40] J.N. Mohapatra, Y. Kamada, H. Kikuchi, S. Kobayashi, J. Echigoya, D.G. Park, Y.M. Cheong, Study of thermal ageing behaviour of Fe–Cr model alloys by magnetic hysteresis loop technique, J. Phys. Conf. Ser. 266 (2011), doi:10.1088/1742-6596/266/1/012041.
- [41] J.N. Mohapatra, Y. Kamada, H. Kikuchi, S. Kobayashi, J. Echigoya, D.G. Park, Y.M. Cheong, Effect of Cr-rich phase precipitation on magnetic and mechanical properties of Fe-20% Cr alloy, IEEE Trans. Magn. 47 (2011) 4356–4359, doi:10.1109/TMAG.2011.2155047.
- [42] J.N. Mohapatra, Y. Kamada, H. Kikuchi, S. Kobayashi, J. Echigoya, D.G. Park, Y.M. Cheong, Evaluation of embrittlement in isochronal aged Fe–Cr alloys by magnetic hysteresis loop technique, J. Magn. 16 (2011) 173–176, doi:10.4283/JMAG.2011.16.2.173.
- [43] J.B.J. Chapman, P.W. Ma, S.L. Dudarev, Dynamics of magnetism in Fe–Cr alloys with Cr clustering, Phys. Rev. B 99 (2019) 184413, doi:10.1103/PhysRevB.99.184413.
- [44] O.C. Hellman, J.A. Vandenbroucke, J. Rüsing, D. Isheim, D.N. Seidman, Analysis of three-dimensional atom-probe data by the proximity histogram, Microsc. Microanal. 6 (2000) 437–444, doi:10.1007/s100050010051.
- [45] S. Küchler, V. Vojtech, S.S.A. Gerstl, R. Schaublin, J.F. Löffler, Thermally decomposed binary Fe–Cr alloys: towards a quantitative relationship between strength and structure, Adv. Eng. Mater. 24 (2022) 1–14 202100909, doi:10.1002/adem.202100909.
- [46] E. Ruska-Centre, FEI Titan 60-300 HOLO, J. Large-Scale Res. Facil. 2 (2016), doi:10.17815/jlsrf-2-70.
- [47] S.L.Y. Chang, C. Dwyer, C.B. Boothroyd, R.E. Dunin-Borkowski, Optimising electron holography in the presence of partial coherence and instrument instabilities, Ultramicroscopy 151 (2015) 37–45, doi:10.1016/j.ultramic.2014.11.019.
- [48] A. Kovács, R.E. Dunin-Borkowski, Magnetic imaging of nanostructures using off-axis electron holography, Handb. Magn. Mater. 27 (2018) 59–153, doi:10.1016/bs.hmm.2018.09.001.
- [49] W.O. Saxton, T.J. Pitt, M. Horner, Digital image processing: the semper system, Ultramicroscopy 4 (1979) 343–353, doi:10.1016/S0304-3991(79)80044-3.
- [50] A. Vansteenkiste, J. Leliaert, M. Dvornik, M. Helsen, F. Garcia-Sanchez, B. Van Waeyenberge, The design and verification of MuMax3, AIP Adv. 4 (2014), doi:10.1063/1.4899186.
- [51] M. De Graef, 2. Lorentz microscopy: theoretical basis and image simulations, Exp. Methods Phys. Sci. 36 (2001) 27–67, doi:10.1016/S1079-4042(01)80036-9.
- [52] <http://quantumandclassical.com/excalibur/>
- [53] P. David, M. Heath, Ferromagnetic resonance absorption and anisotropy of chromium iron alloys, J. Phys. Colloques 32 (1971) 112–113, doi:10.1051/jphyscol:1971135.

- [54] T. Kubota, J. Hamrle, Y. Sakuraba, O. Gaier, M. Oogane, A. Sakuma, B. Hillebrands, K. Takanashi, Y. Ando, Structure, exchange stiffness, and magnetic anisotropy of $\text{Co}_2\text{MnAlxSi}_{1-x}$ Heusler compounds, *J. Appl. Phys.* 106 (2009) 1–4, doi:[10.1063/1.3265428](https://doi.org/10.1063/1.3265428).
- [55] J.W. Cahn, J.E. Hillard, Free energy of a nonuniform system. I. Interfacial free energy, *J. Chem. Phys.* 28 (1958) 258–267, doi:[10.1063/1.1730145](https://doi.org/10.1063/1.1730145).
- [56] A.T. Aldred, Ferromagnetism in iron-chromium alloys. I. Bulk magnetization measurements, *Phys. Rev. B* 14 (1976) 219–227, doi:[10.1103/PhysRevB.14.219](https://doi.org/10.1103/PhysRevB.14.219).
- [57] A.T. Aldred, B.D. Rainford, J.S. Kouvel, T.J. Hicks, Ferromagnetism in iron-chromium alloys. II. Neutron scattering studies, *Phys. Rev. B* 14 (1976) 228–234, doi:[10.1103/PhysRevB.14.228](https://doi.org/10.1103/PhysRevB.14.228).
- [58] J.F. Löffler, H.B. Braun, W. Wagner, G. Kostorz, A. Wiedenmann, Magnetization processes in nanostructured metals and small-angle neutron scattering, *Phys. Rev. B Condens. Matter Mater. Phys.* 71 (2005) 1–15, doi:[10.1103/PhysRevB.71.134410](https://doi.org/10.1103/PhysRevB.71.134410).
- [59] J.F. Löffler, H.B. Braun, W. Wagner, Magnetic correlations in nanostructured ferromagnets, *Phys. Rev. Lett.* 85 (2000) 1990–1993, doi:[10.1103/PhysRevLett.85.1990](https://doi.org/10.1103/PhysRevLett.85.1990).